# DESIGN ASPECTS OF A MAGNETICALLY GEARED PERMANENT MAGNET MACHINE WITH AN OUTER-STATOR

**PM Tlali, JDG van der Merwe, R-J Wang, S Gerber** *

* *Department of Electrical & Electronic Engineering, Stellenbosch University, Private Bag X1, Matieland 7602, South Africa, E-mail: 15894215@sun.ac.za; rwang@sun.ac.za; sgerber@sun.ac.za*

**Abstract:** Magnetically geared permanent magnet (MGPM) machines are an attractive alternative for wind power applications because of their merits over other machine types. A prototype MGPM machine was constructed in a recent study. Although both theoretical and finite element methods predict high efficiencies on the design, the prototype's practical measurements differ to them by a significant margin due to mechanical problems experienced in the manufacturing process. This paper discusses some of the design improvements done on a previously designed and built machine prototype. It focuses mainly on the mechanical aspects of it, and has shown that careful consideration on that sector can help improve its efficiency.

**Key words:** Magnetically geared machines, permanent magnets, magnetic flux modulation.

## 1. INTRODUCTION

The constant increase in the demand of energy worldwide coupled with environmental concerns has been the major drive for rapid development in renewable energy power generation. Amongst others, wind energy has become one of the most promising renewable energy sources. There exists several different generator drive-train configurations for harvesting wind power. Two most common configurations are mechanically geared medium or high speed generator system and low speed directly driven generator (DDG) systems.

Although the mechanically geared high speed generator system enjoys the advantages such as an improved efficiency [1, 2], compact and light weight, the reliability of the mechanical gearbox is still a major concern. Since the mechanical gearbox relies on physical teeth meshing mechanism for torque transfer, it is noisy and subject to wear. In addition, in the event of overload conditions, mechanical gearbox can easily be damaged. Therefore, condition monitoring and frequent maintenance are necessary, which is a challenging task especially in the offshore plants. On the other hand, the DDGs are more reliable and have less complex mechanical structure. But, the size and weight of the DDGs increase rapidly with high power rating [3].

As an alternative to the two common configurations currently implemented, magnetically geared permanent magnet (MGPM) machines have recently been proposed for wind power application [4–6]. The MGPM machines are essentially a combination of a coaxial flux modulated magnetic gear (CMG) and a conventional medium to high speed permanent magnet synchronous machine (PMSM). This enables a direct connection of the low-speed high-torque turbine onto the machine without an external gearbox. The whole system potentially can be light weight and small volume. Furthermore, because of the non-contact gearing principle of CMG, MGPM machines

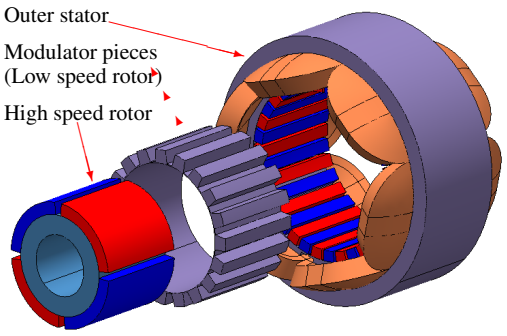


Figure 1: Outer-stator MGPM machine structure.

boast several advantages such as [4–6]: (i) quiet operation, (ii) inherent overload protection, (iii) little maintenance, and (iv) potential for high torque density and efficiency.

In an attempt to practically validate the potential merits of such a machine, the authors had previously designed and built a prototype of an outer-stator MGPM (OS-MGPM) machine for use in the wind power generation [7]. The machine showed satisfactory output characteristics as expected, and exhibited good efficiency from the finite element analysis (FEA) based computer simulations. It was however found that the mechanical losses had the major contribution to the machine's total losses. Moreover, the stator winding had a lower than designed fill factor due to difficulties in the winding process.

The main aim of this paper is to revisit the design and construction of the previously built OS-MGPM machine prototype. It is envisaged that with the improvement on both the electromagnetic and mechanical design aspects, the overall machine's losses can be significantly reduced resulting in improved efficiency.

## 2. MACHINE DESCRIPTION

The system layout of the OS-MGPM machine investigated is shown in Fig. 1. It consists of the following main components: the high-speed inner PM rotor, ferromagnetic low-speed flux modulator and an outer-stator with tooth concentrated non-overlapping windings. A set of PMs is also glued to on the inner surface of the stator.

In the same manner as in CMGs, the working principle of the OS-MGPM machine is based on the fact that the ferromagnetic pole-pieces modulate the magnetic fields from both sets of PMs. Then the PMs on either side of the modulator engages with the field harmonics of the same order to their pole-pair number. In this way, the magnetic torque is transferred between the two PMs sets and the modulator, two of them running at different speeds while one is fixed, forming the gearing action. Furthermore, the fundamental field harmonics from the inner PM rotor together with the stator PMs' modulated fields interacts with the stator windings to produce electrical power. For the magnetic gearing phenomena to take place, the number of PM pole pairs on the inner- and outer-rotors, $p_h$ and $p_l$ respectively, and the modulator pole-pieces ($q_m$) are related by the following equation [8,9]:

$$q_m = p_l \pm p_h \tag{1}$$

And with the other set of stationary PMs fixed on the stator, the speed gearing ratio $G_r$ between the inner PM rotor and the flux modulator is given by:

$$G_r = \frac{\omega_h}{\omega_m} = \frac{q_m}{p_h} \tag{2}$$

where $\omega_m$ and $\omega_h$ are modulator and inner rotor's speeds, respectively.

The employed electromagnetic design environment, main machine dimensions and other parameters are kept the same as in the previous prototype [7]. Most of the proposed changes were focused on the mechanical aspects of this machine. For the sake of clarity, the redesigned machine's key specifications are provided in Table 1.

Table 1: Machine key parameters.

| | **Parameter Description** | **Value** |
|---|---|---|
| OS-MGPM | Outer diameter | 140 mm |
| | Stack length | 50 mm |
| | Air-gap lengths | 0.7 mm |
| | Magnet remanence | 1.39 T |
| | PM relative perm. | 1.05 |
| | Lamination material | M470-50A |
| Generator | Number of slots | 6 |
| | Number of poles | 4 |
| | Number of phases | 3 |
| | Winding layers | 2 |
| | Rated frequency | 52.5 Hz |
| | Winding factor | 0.866 |
| Gear | Inner rotor pole-pairs | 2 |
| | Fixed PM pole-pairs | 19 |
| | Modulator pole-pieces | 21 |
| | Gearing ratio | 10.5 |
| | Rated speed | 150 rpm |

## 3. DESIGN IMPROVEMENTS

### *3.1 Shaft Design*

The shaft design process included an examination into the following elements: material selection, geometric layout, stress and strength, deflection and rigidity and vibration due to natural frequency. Critical areas were located and analyzed so as to meet the requirements of the shaft supported elements.

The shaft layout of the machine consists of the modulator and inner rotor coupled by the bearings as shown in Fig. 2, together with its free body diagram. To avoid complications imposed by this layout on static force analysis, the shaft components were grouped as one since the force will act simultaneously on both of them. But the torsional stress analysis due to rotational forces is done on the modulator shaft alone. The combination of the resultant forces acting on the shaft components and the machine's total weight obtained from 3D FEA is represented by $F_y$ in the diagram. Then the corresponding resultant forces ($F_{Ay}$ and $F_{By}$) at points A and B can be calculated by making use of equilibrium principle. In the diagram, the point 'C' is identified as the most vulnerable shaft point because it has the smallest diameter, and both torsional and bending stresses are more effective on that region. The selected shaft material was cold

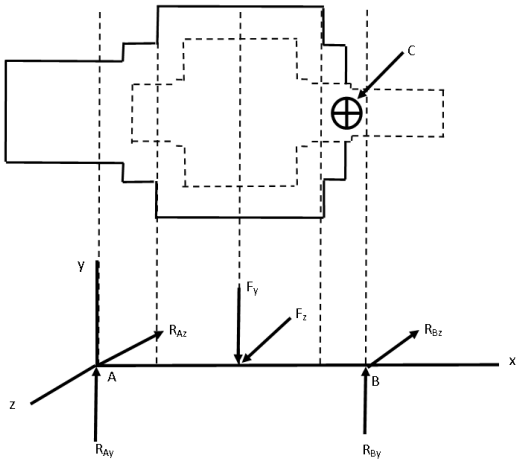


Figure 2: Combined shaft free body diagram.

drawn mild steel, grade 080M40, with the properties given in Table 2. Different types of stresses have been combined into mid-range von Mises stress equations, which is customized for shaft applications. For a solid and circular cross-section shaft with inertial geometry terms

Table 2: Shaft material properties

| | | | |
|---|---|---|---|
| Hardness HB | 108 | Modulus of elasticity E (GPa) | 895 |
| Tensile strength (MPa) | 700 | True strain at fracture | 0.96 |
| Fatigue strength exponent b | -0.12 | Fatigue strength coefficient $\sigma_f$ (MPa) | 465 |
| Fatigue ductility coefficient $\varepsilon_F$ | 0.22 | Fatigue ductility exponent c | -0.66 |

incorporated, these equations are expressed as [10]:

$$\sigma_a = K_f \frac{32M_a}{\pi d^3} \qquad \sigma_m = K_f \frac{32M_m}{\pi d^3} \tag{3}$$

$$\tau_a = K_{fs} \frac{16T_a}{\pi d^3} \qquad \tau_m = K_{fs} \frac{16T_m}{\pi d^3} \tag{4}$$

where $M_a$ and $M_m$ represents the mid-range and alternating bending moments, $K_f$ and $K_{fs}$ are fatigue stress concentration factors for bending and torsion, $T_m$ and $T_a$ are the mid-ranges and alternating torques, respectively, and d is the shaft diameter.

The maximum bending moment $M_{max}$ occurs in the x-y axis (see Fig. 2), due to machine's weight, while axial forces are ignorable. The torque values obtained from electromagnetic FEA are given in Table 3.

Table 3: Torque values from electromagnetic FEA

| | | | |
|---|---|---|---|
| $M_a$ | 1.0518 Nm | $M_{max}$ | 82.26 Nm |
| $T_m$ | 70 Nm | $M_m = T_a$ | 0 |

The fatigue stress concentration factors $K_f$ and $K_{fs}$ are respectively reduced from $K_t$ and $K_{ts}$, which are obtained from the geometry and material specifications of the used shaft [10]. Equations (3) and (4) are then combined with the distortion energy failure theory of the von Mises stresses. For a solid and round rotating shaft, with axial loads neglected, these are calculated with equations below [10]:

$$\sigma'_a = \left(\sigma_a^2 + 3\tau_a^2\right)^{1/2} = \sqrt{\left(\frac{32K_f M_a}{\pi d^3}\right)^2 + 3\left(\frac{K_{fs}16T_a}{\pi d^3}\right)^2} \tag{5}$$

$$\sigma'_m = \left(\sigma_m^2 + 3\tau_m^2\right)^{1/2} = \sqrt{\left(\frac{32K_f M_m}{\pi d^3}\right)^2 + 3\left(\frac{K_{fs}16T_m}{\pi d^3}\right)^2} \tag{6}$$

Equations (3) - (6) are used together with the values of the analyzed machine in Table 3, the following results are obtained. Using the modified Goodman diagram, the failure curve of these alternating and midrange stresses can be evaluated, with fatigue failure criteria defined as [10]:

$$\frac{1}{n_f} = \frac{\sigma'_a}{S_e} + \frac{\sigma'_m}{S_{ut}} \tag{7}$$

where $S_{ut} \geq 1400$ MPa. Since the modified Goodman criteria does not guard against yielding, separate check was incorporated. A von Mises maximum stress ($\sigma_{max}$) is

Table 4: Shaft design factors

| | | | |
|---|---|---|---|
| $K_t$ | 1.6 | $q_{shear}$ | 0.93 |
| $K_{ts}$ | 1.35 | $\sigma_a$ | 2.014 MPa |
| $K_f$ | 1.504 | $\tau_m$ | 74.14 MPa |
| $K_{fs}$ | 1.294 | $\sigma'_a$ | 2.014 MPA |
| q | 0.84 | $\sigma'_m$ | 128.4 MPA |

calculated and then compared to the yield strength $S_y$ (see eqn: (9)):

$$\begin{aligned}\sigma'_{max} &= \left[(\sigma_m + \sigma_a)^2 + 3(\tau_m + \tau_a)^2\right]^{1/2} \\ &= \sqrt{\left(\frac{32K_f(M_m + M_a)}{\pi d^3}\right)^2 + 3\left(\frac{K_{fs}16(T_m + T_a)^2}{\pi d^3}\right)^2}\end{aligned} \tag{8}$$

$$n_y = \frac{S_y}{\sigma'_{max}} \quad > \quad \frac{S_y}{\sigma'_a + \sigma'_m} \tag{9}$$

For steels of up to 1450 MPa, it is suggested that the endurance limit ($S'_e$) be in the ranges of 40 % to 60 % of the steel's tensile strength [10]. The endurance in the case of this prototype analysis is estimated to be 50 % of the tensile strength, i.e $S'_e = 0.5S_{ut}$. The Marin equation ($S_e$) was further employed to take into account various influences that different factors may have on the endurance limit. It includes quantified effects of the surface factor, size, loading, temperature and miscellaneous items [10].

$$S_e = k_a k_b k_c k_d k_e k_f S'_e \tag{10}$$

where $k_a$ is the surface conditioning factor, $k_b$ is dedicated to the sizing factor, $k_c$ is the load factor, $k_d$ is the temperature factor and $k_e$ the reliability factor.

The reliability factor is the probability that a known stress will exceed the strength of a randomly selected component that is manufactured out of the same material. In the foregoing design, both $k_c$ and $k_e$ have been approximated as 1. The other factors are defined by the equations below, and their calculated values are given in Table 5.

$$\begin{aligned}K_a &= aS_{ut}^b \\ K_b &= \left(\frac{d}{7.62}\right)^{-0.107} \\ K_d &= 0.9877 + 0.6507(10^{-3})T_C - 0.3414(10^{-5})T_C^2 \\ &\quad + 0.5621(10^{-8})T_C^3 - 0.6246(10^{-12})T_C^4\end{aligned} \tag{11}$$

The modified Goodman fatigue failure criteria can be

Table 5: Marin equation factors values

| | | | |
|---|---|---|---|
| $S_{ut}$ | 700 MPa | $K_a$ | 0.795 |
| $S'_e$ | 350 MPa | $K_b$ | 0.902 |
| $S_e$ | 253 MPa | $K_d$ | 1.009 |

calculated from a combination of these results, while the fatigue factor $n_f$ and the yielding factor $n_y$ are evaluated from eqns (7) and (9). The values for these factors are provided in Table 6 for the designed shaft. It can be clearly seen that yield factor for the old shaft $n_{y,shaft}$ is less than

the maximum yield factor $n_{y,max}$. However, these factors are too high and indicate that the shaft was over-designed for the expected loads. The safety factor of the old shaft was 5.22, whereas it is expected to be 1.5 - 2.

Table 6: Shaft's Goodman fatigue factors

| | | | |
|---|---|---|---|
| $\sigma'_{max}$ | 128.4 MPa | $n_{y,max}$ | 3.62 |
| $n_f$ | 5.22 | $n_{y,shaft}$ | 3.565 |

### 3.2 Bearing Selection

Stresses occur on both the inner- and outer-rings of a ball bearing as a result of its rolling mechanism of operation. The bearing life, defined as the total number of revolutions that it can withstand before it can fail or fatigue can be developed, is termed rating life. With the intended bearing life ($L_D$), predicted radial load ($F_D$) to withstand, and desired rotational speed ($n_D$) all known, the catalogue rating ($C_{10}$) can be calculated from eqn (12). The parameter ($C_{10}$) is then used to select a suitable bearing for certain application.

$$C_{10} = F_D \left( \frac{L_D n_D 60}{L_R n_R 60} \right)^{1/a} \tag{12}$$

where $n_R$ is rated speed, $L_R$ is rated life and $a = 3$ for ball bearings.

It was then realized that the old machine had oversized bearings. Since the bearing losses are directly proportional to its bore diameter, oversized bearings could unreasonably add more losses as smaller bearings could have been used instead. Furthermore, SKF energy efficient ball bearings were used instead of normal ball bearings as it was the case with old machine, which then have a potential of 10% bearing loss reduction. From the used bearing specifications in Table 7, it can be seen that the new bearings have small bore diameters while they can still handle almost equal load as the old ones.

Table 7: Bearing specifications

| **Bearing designation** | **Inner D(mm)** | **Outer D(mm)** | **Width (mm)** | **Load (kN)** |
|---|---|---|---|---|
| E2.6302-2Z | 15 ↓ | 42 | 13 | 11.4 |
| 6004-2RSH | 20 | 42 | 12 | 9.95 |
| E2.6303-2Z | 17 ↓ | 47 | 14 | 13.8 |
| 6005-2RSH | 25 | 47 | 12 | 11.9 |
| E2.6204-2Z | 20 ↓ | 47 | 14 | 12.7 |
| 6005-2RSH | 25 | 47 | 12 | 11.9 |
| E2.6208-2Z | 40 ↓ | 80 | 18 | 30.7 |
| 6009-2RS1 | 45 | 75 | 16 | 22.1 |

↓ Indicates reduced bearing bore diameter.

### 3.3 Stator Winding

The stator coils were re-wound in an attempt to improve the fill-factor and reduce the end-windings' length. Due to the same winding challenges previously met in the process during the first trial, the newly realized coils had 10 turns less than the old. On the other hand, the end-winding's lengths seemed to be much shorter as they were pulled tighter. The shorter end-windings' length promises less machine's total resistance. This clearly shows that closed-slots stator brings manufacturing challenges which could also be detrimental to the machine's performance. In this regard, alternative stator configurations (e.g. segmented stator) should be considered.

## 4. TESTING AND RESULTS

### 4.1 Bearing Losses

A test model was developed to measure the losses for each bearing individually without the interference of magnetic and electromagnetic active parts of the machine. This was done with the aim of separating the no-load core losses from mechanical losses. Unfortunately, only the big bearing's (E2.6208-2Z) losses were accurately measured due to the model's and measuring equipments' limitations. Hence, the amount of loss contribution of the other three bearings was still unknown. Figure 3 shows the comparison of the old and new big bearings' losses, together with their theoretical predictions. It can be seen that there is a huge difference between the practical losses of the two bearings. For a machine with such a small output capacity, this can directly be reflected by the reduced overall efficiency.

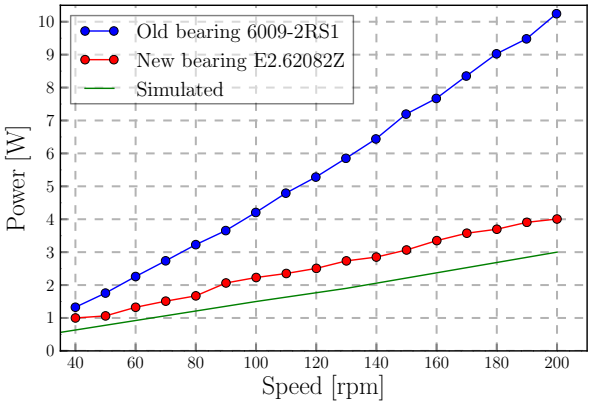


Figure 3: Comparison of two bearings' losses.

### 4.2 Stator Resistance

In order to find a practical value of the stator resistance, and check whether the three phases are properly balanced, a DC coil resistance test was done. The average per-phase resistance was found to be 5.8 Ω, which is 1.5 Ω less than that of the previous windings, as presented in Table 8. Although the current number of coil turns is slightly less than before, the big difference in the resistances is a result of shortened end-windings' lengths. It is believed that this will have a significant reduction in copper losses.

Table 8: Stator resistances

| Old stator | New stator | Difference |
|---|---|---|
| 7.3 Ω | 5.8 Ω | 1.5 Ω |

### 4.3 *No-load Losses*

In order to see if the implemented changes did improve on the machine's performance, no-load loss tests were conducted. This was done with the machine's terminals open so that only the eddy current, hysteresis and mechanical losses can be measured, while excluding copper loss.

A comparison of these losses as predicted from FEA, and measured from the first and re-designed machines is given in Fig. 4. There is a big difference between FEA predicted and measured losses. However, the difference between the two versions of the machine is not significant. This can be attributed to the fact that the three other bearings running at high speed were not replaced since the proposed new bearings could not be acquired. It is understood that the losses would have drastically reduced if the energy efficient bearings with smaller bore diameters were used instead.

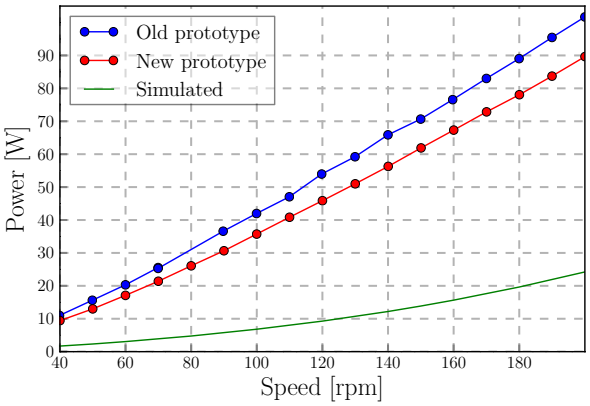


Figure 4: No-load loss comparison.

### 4.4 *Open Circuit Voltage*

By operating the prototype machine as a generator under no-load conditions, the induced back electro-motive force (EMF) was obtained. The stator EMF waveforms measured at an input speed of 150 rpm are plotted in Fig. 5. They are balanced in both the magnitude and phase displacement, proving that the stator windings were correctly configured. Furthermore, the output electrical frequency ($f_e$) is obtained to be 52.5 Hz, which is in good agreement with the theoretical calculations. Therefore, the speed and/or torque gearing principle can also be validated by calculation of the inner rotor's mechanical speed ($n_h$) from $f_e$ and then comparing it to the input speed, as shown

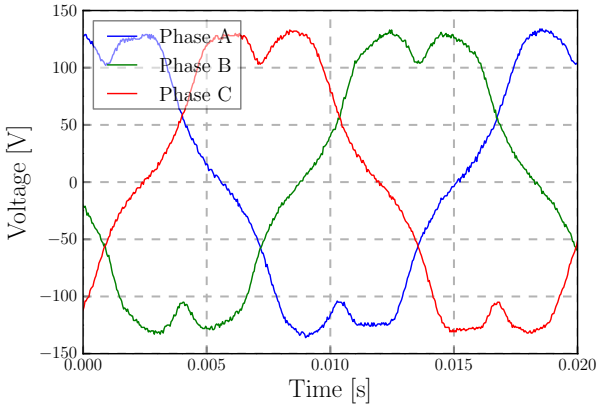


Figure 5: Electromotive force waveforms at 150 rpm.

below:

$$n_h = \frac{60 \times f_e}{p_h} = \frac{60 \times 52.5}{2} = 1575\,rpm \qquad (13)$$

And the gear ratio is:

$$G_r = \frac{n_h}{n_l} = \frac{1575}{150} = 10.5 \qquad (14)$$

where $n_h$ and $n_l$ are output and input speeds, respectively. A graph of open circuit voltage as a function of input speed is given on Fig. 6. From this, the practical machine's induction constant ($k_m$) is found to be 0.86. Also, the FEA simulated magnitudes are slightly higher than the experimental measurements due to 3D end effects.

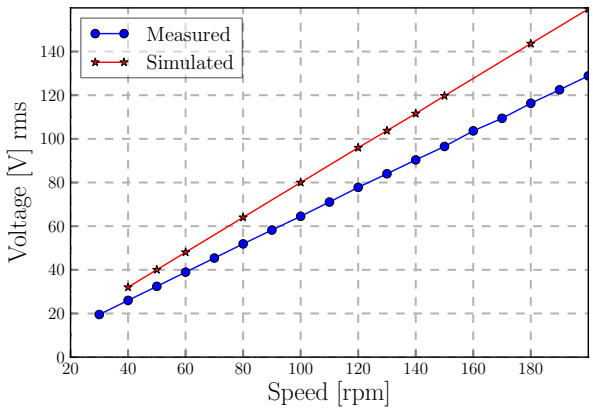


Figure 6: Phase rms voltage as a function of speed.

### 4.5 *Load Tests*

The output efficiency of the machine was determined by measuring the input mechanical and output electrical power at various operating speeds. Both the output active power and efficiency at rated current are presented in Fig. 7, as a function of speed and at two different constant loads. Since the power graph is plotted at a constant current, this means the copper losses are also fixed, hence

the efficiency has an increasing trend with increase in speed. The slope of an efficiency graph is initially steeper but flattens at higher speeds due to overwhelming friction and core losses.

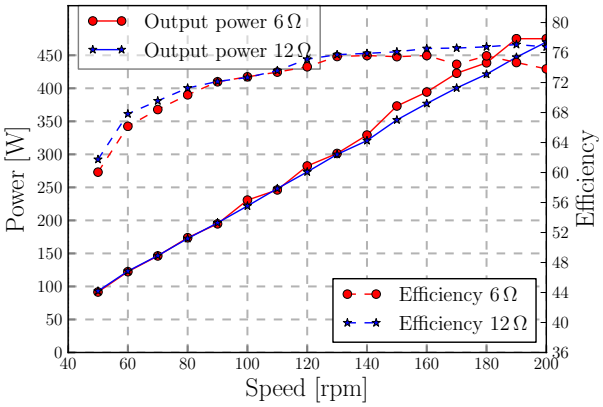


Figure 7: Output power and efficiency at rated current.

### 4.6 *Overload Condition*

The pull-out or slip torque of the machine is measured by overloading it until it's gear-part slips or becomes un-synchronized. Figure 8 illustrates the torque on the input side (modulator) as a function of time while the load is steadily increased. It can be seen that the torque increases until the gear slips at almost 60 Nm, which is actually the machine's stall torque predicted by FEA [7]. After the slip point, the torque oscillates between positive and negative magnitudes until the load is decreased well below its capability and the gear re-engages. The over-load condition occurs at almost twice the rated current. This further demonstrates the overload protection characteristic of the MGPM machines.

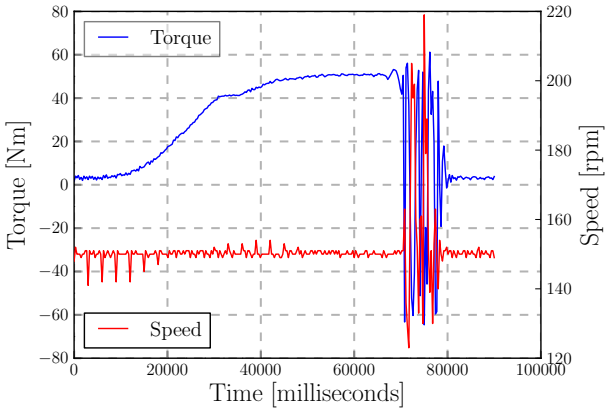


Figure 8: Overload test to illustrate machine's pullout torque.

## 5. CONCLUSIONS

In this paper, design improvements for an MGPM machine prototype were proposed and implemented. It has been shown that careful consideration on the non-electromagnetic active components such as bearings and shaft can considerably reduce the losses. The over-load protection and contact-less power transmission are clearly the advantages of MGPM machines comparing with mechanically geared systems. However, to fully realize the superiority of these machines, the mechanical design optimization is just as important as the electromagnetic design.

## REFERENCES

[1] H. Polinder, F.F.A. van der Pijl, G-J. de Vilder, P.J. Tavner, "Comparison of direct-drive and geared generator concepts for wind turbines," IEEE Trans. Energy Convers., 21(3):725-733, Sept. 2006.

[2] R.-J. Wang, S. Gerber, "Magnetically geared wind generator technologies: Opportunities and challenges," Appl. Energy, vol. 136:817-826, Dec. 2014.

[3] D. McMillan, G.W. Ault, "Techno-economic comparison of operational aspects for direct drive and gearbox-driven wind turbines," IEEE Trans. Energy Convers., 25(1):191-198, Mar. 2010.

[4] K.T. Chau, D. Zhang, J.Z. Jiang, C. Liu, Y. Zhang, "Design of a magnetic-geared outer-rotor permanent-magnet brushless motor for electric vehicles," IEEE Trans. Magn., 43(6):2504-2506, Jun. 2007.

[5] K. Atallah, S. Calverley, R. Clark, J. Rens, D. Howe, "A new PM machine topology for low-speed, high-torque drives," in Proc. 18th Int. Conf. Elect. Mach. (ICEM), Vilamoura, Portugal, Sep. 2008, pp. 1-4.

[6] L. Jian, K.T. Chau, J.Z. Jiang, "A magnetic-geared outer-rotor permanent-magnet brushless machine for wind power generation," IEEE Trans. Ind. Appl., 45(3):954-962, May/Jun. 2009.

[7] P.M. Tlali, S. Gerber, R-J. Wang, "Optimal design of an outer-stator magnetically geared permanent magnet machine," IEEE Trans. Magn., (early access).

[8] K. Atallah, D. Howe, "A novel high performance magnetic gear," IEEE Trans. Magn., 37(4):2844-2846, Jul. 2001.

[9] K. Atallah, J. Wang, D. Howe, "A high performance linear magnetic gear," J. Appl. Phys., 97(10):10N516-110N516-3, May 2005.

[10] R.G. Budynas, J.K. Nisbett, *Shigley's Mechanical Engineering Design*, McGraw-Hill, 2008.